High-Temperature Ionic Epitaxy of Halide Perovskite Thin Film and the Hidden Carrier Dynamics

*Yiping Wang, Xin Sun, Zhizhong Chen, Yi-Yang Sun, Shengbai Zhang, Toh-Ming Lu, Esther Wertz, and Jian Shi**

High-temperature vapor phase epitaxy (VPE) has been proved ubiquitously powerful in enabling high-performance electro-optic devices in III–V semiconductor field. A typical example is the successful growth of p-type GaN by VPE for blue light-emitting diodes. VPE excels as it controls film defects such as point/interface defects and grain boundary, thanks to its high-temperature processing condition and controllable deposition rate. For the first time, single-crystalline high-temperature VPE halide perovskite thin film has been demonstrated—a unique platform on unveiling previously uncovered carrier dynamics in inorganic halide perovskites. Toward wafer-scale epitaxial and grain boundary-free film is grown with alkali halides as substrates. It is shown the metal alkali halides could be used as universal substrates for VPE growth of perovskite due to their similar material chemistry and lattice constant. With VPE, hot photoluminescence and nanosecond photo-Dember effect are revealed in inorganic halide perovskite. These two phenomena suggest that inorganic halide perovskite could be as compelling as its organic–inorganic counterpart regarding optoelectronic properties and help explain the long carrier lifetime in halide perovskite. The findings suggest a new avenue on developing high-quality large-scale single-crystalline halide perovskite films requiring precise control of defects and morphology.

The surge in research interest and rapid advances[1–3] concerning halide perovskite (ABX_3) in recent years has quickly pushed the material family to a close proximity of the achievements of conventional semiconductors like the Group IV (Si, Ge), III–V (GaN, GaAs), and II–VI (ZnO, CdTe) materials.[4] In the fields of photovoltaic,[5–8] electro-optics,[9–11] and optoelectronics,[12,13] high-performance devices composed of either hybrid or pure inorganic halide perovskite have been demonstrated as a competitive potential substitute for their counterparts based on traditional semiconducting materials. However, as is the case for every material family, a real prosperity cannot live without a success of high-quality thin film growth, among which typical examples would be the growth of p-type GaN for blue light-emitting diode (LED)[14] and high-temperature Fe-based superconductor.[15] Halide perovskite in such aspect still falls quite far behind since so far polycrystalline film remains to be mostly used in devices, whereas advanced and matured techniques including vapor phase epitaxy (VPE) can produce high-quality single-crystalline IV, III–V, or II–VI thin films for designed application purposes.[4,16] Currently, the large-scale monocrystalline growth of halide perovskite has been limited to solution-based method[17–23] that ends up with bulk crystal or film with dimension/morphology limited by the physical molds applied. High-temperature VPE techniques, compared to the low-temperature solution-based ones, have been shown very effective in morphology control, and more importantly, reducing varieties of kinetically induced defects in growing conventional semiconductors.[24] Decades of experience with conventional materials have determined the suitable substrates for monocrystalline film growth—a key step for VPE—like silicon and sapphire wafers for group IV and III–V,[4] while very limited progress has been made in the halide perovskite field. A direct consequence of such shortcoming is the absence of high-quality epitaxial halide perovskite film, an issue unable to be circumvented for the rising of the perovskite family as a real competitor for conventional semiconductors.

The presence of both alkali and halide elements has made halide perovskite radically different from conventional semiconductors in that significant ionicity exists in the material's bonding nature. This means that upon choosing the substrate, the chemical wetting of the elements in perovskite on the substrate surface would be equally or more important than the "traditional" thoughts about lattice constant and symmetry. Previous works on van der Waals epitaxy of halide perovskite on muscovite mica substrate[25–27] demonstrate that even with huge lattice mismatch and completely different lattice type, ordering perovskite flakes/nanowires could still be achieved. Such experimental results led us to focus on the potassium layer on the mica cleavage plane,[28,29] which could provide good wetting for the A site element of the perovskite material. Per such considerations, we hope to find substrates readily available while being "similar" with the halide perovskite. A most direct candidate

---

Y. Wang, Z. Chen, Prof. J. Shi
Department of Materials Science and Engineering
Rensselaer Polytechnic Institute
Troy, NY 12180, USA
E-mail: shij4@rpi.edu

Dr. X. Sun, Dr. Y.-Y. Sun, Prof. S. Zhang, Prof. T.-M. Lu, Prof. E. Wertz
Department of Physics
Applied Physics, and Astronomy Rensselaer Polytechnic Institute
Troy, NY 12180, USA

DOI: 10.1002/adma.201702643

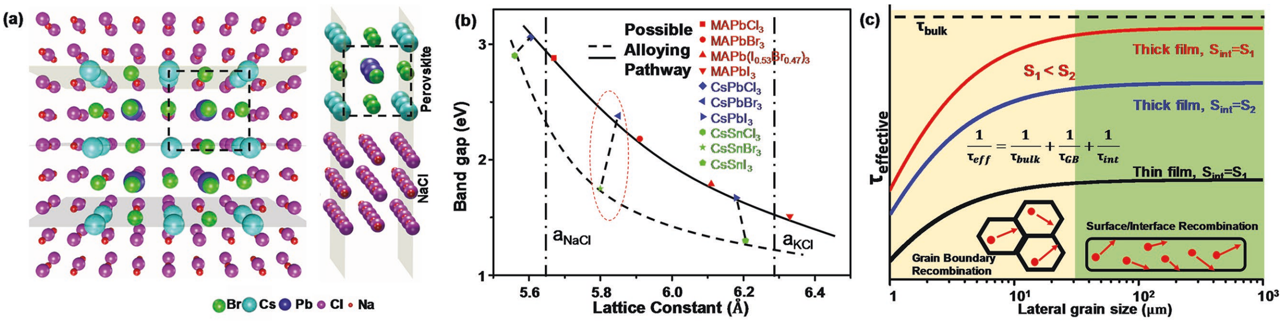

Figure 1. Theoretical guidelines for vapor phase epitaxy (VPE) of halide perovskite on alkali halides. a) Atomic model of (001) $CsPbBr_3$ perovskite on (001) NaCl for both top view (left) and front view (right). The two lattices show good registration at the interface. b) Plot of lattice constants versus band gap for the halide perovskite family including both hybrid (red legends), pure inorganic (blue legends), and Sn (green legends) based perovskites, which covers the entire visible light range. The lattice constants fall within NaCl and KCl range which indicates that NaCl and KCl would be suitable for the ionic epitaxial growth of halide perovskite. The possible alloying pathways for realizing tunable band gaps are also marked on the map by both solid and dashed lines. c) Plot of effective lifetime versus lateral grain size and vertical thickness under different carrier recombination rate. Generally recombination at grain boundaries and interfaces lower the lifetime, while a faster recombination rate also leads to shorter lifetime. The schematics show, respectively, the regime where grain boundary/interface affects most the final measured lifetime.

would be the alkali halides, with the prototypical example being the table salt NaCl. Compared with halide perovskite, NaCl possesses the same cubic symmetry, a close lattice constant, and very similar chemical properties derived from their ionic nature (close melting point, easy cleavage, water solubility). **Figure 1**a shows the top (left inset) and side (right inset) views of the superposition of perovskite $CsPbBr_3$ on top of cubic NaCl (001) surface. It can be observed that with $CsPbBr_3$ (001)||NaCl (001), the two lattices have good registration and more importantly, for the first layer of perovskite to wet on the NaCl, the Cs and Br elements would get easily bounded to the corresponding alkali and halide positions. A further demonstration of the universality of the use of alkali halide substrates for halide perovskite growth, is shown in Figure 1b, where the lattice constant and band gap of different halide perovskites (Pb and Sn based, both hybrid and inorganic) are plotted.[5,19,30–32] Fortunately, we see that halide perovskites, with band gaps ranging from 3.0 to 1.6 eV, mostly fall within the lattice constants of NaCl and KCl, the two most common alkali halides. Figure 1b shows that the alkali halide substrate is suitable for the growth of various types of perovskite material depending on the lattice mismatch, that is, NaCl for Cl and Br-based perovskite and KCl for I-based one. Such scenario is in great resemblance to the matured system of AlN-GaN-GaAs-InAs,[4,24] where AlN buffered sapphire and 6H-SiC substrates are generally used. Also displayed in Figure 1b are the possible alloying pathways for all A, B, and X sites (solid line: experimentally achieved;[31,33] dashed line: hypothesized) for manipulation of tunable band gaps, which has also been widely employed in the matured material system. Specifically, we can see that with a considerable band gap offset of ≈0.5 eV, $CsPbBr_3$ and $CsSnBr_3$ have a small lattice mismatch, which would be an ideal case for B-site alloying.

The advantages brought about by the realization of large-scale VPE thin film to the actual exploration and application of halide perovskite are immense. So far for polycrystalline films, defects (point defects, grain boundaries, interphase defects) have limited the material properties like carrier mobility and lifetime and would act as possible red herrings for the revelation of the intrinsic properties behind.[34,35] Figure 1c semi-quantitatively plots the effect of grain size and thickness on the effective lifetime of halide perovskite, one of the key factors affecting the device performance. By taking into account the interfacial recombination effect from top and bottom for thin film, we modified the effective lifetime equation from previous works[36–38]

$$\frac{1}{\tau_{\text{eff}}} = \frac{1}{\tau_{\text{bulk}}} + \frac{1}{\tau_{\text{GB}}} + \frac{1}{\tau_{\text{Int}}} = \frac{1}{\tau_{\text{bulk}}} + \frac{2}{\frac{d}{2S_{\text{GB}}} + \frac{1}{D}\left(\frac{d}{\pi}\right)^2} + \frac{2}{\frac{t}{2S_{\text{Int}}} + \frac{1}{D}\left(\frac{t}{\pi}\right)^2} \tag{1}$$

where d is the lateral grain size, t the vertical thickness, D the diffusivity, S the recombination velocity, and the subscripts GB and Int denote grain boundary and interface, respectively. By plugging in the recombination velocity and diffusivity for halide perovskite,[37] Figure 1c shows that for small grained polycrystalline film, the average size would significantly affect the lifetime. While for monocrystalline thin film, the recombination at the interfaces becomes the limiting factor. A thicker high-quality film is therefore favored for the study of fundamental physics and intrinsic properties. Under the same material morphology (grain size and thickness), recombination velocity has much influence on the final result, with a slower velocity rendering a longer effective lifetime. For the same material, whereas S_{GB} is fixed, S_{Int} could be significantly different depending on the growth condition (e.g., solution method vs VPE) and interfacial chemistry. Generally, the remnant of solvents and higher defect density from lower temperature growth would result in a higher recombination velocity in solution methods, a major reason why VPE is preferred. The above analysis has assumed an identical diffusivity for both carriers, where in real case the mobility difference would further complicate the matter, one topic we will address in later sections.

Following these rationale, by attempting VPE of pure inorganic $CsPbBr_3$ and $CsSnBr_3$ on NaCl substrate, we demonstrate that single-crystalline thin film with lateral dimension up to

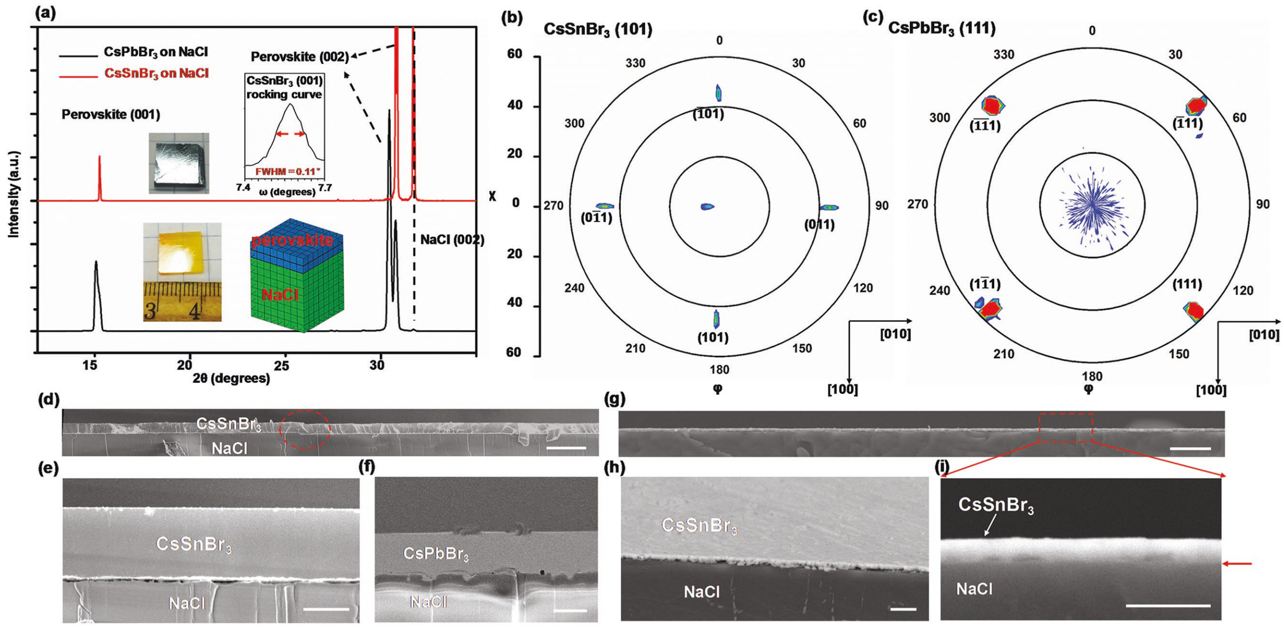

Figure 2. Structure and morphology characterizations of VPE halide perovskite on NaCl. a) θ-2θ XRD analysis of CsSnBr$_3$/NaCl (red) and CsPbBr$_3$/NaCl (black). Both samples show only (100) and higher order peaks parallel to NaCl (002). The left two insets show the camera images of the mirror-like 1 cm × 1 cm film obtained after growth. The right inset shows a (001) rocking curve for CsSnBr$_3$ with a FWHM of 0.11°. b) (110) pole figure of CsSnBr$_3$ showing four distinctive (110) poles, each 90° apart, indicating single-crystal growth. The coordinates on the right bottom corner show the in-plane orientation deduced from the pole figure. c) (111) pole figure of CsPbBr$_3$ which also points to single-crystal film growth. The in-plane orientations are also marked. d–f) SEM images of thicker halide perovskite film. d) Lower magnification image of the CsSnBr$_3$/NaCl cross section. The perovskite film grows uniformly over large scale with conformal coating (marked by the dashed circle) on the surface. e) Higher magnification image at the interface shows the absence of grain boundaries. f) A tilted cross-section view of ≈7 µm CsPbBr$_3$ on NaCl with similar surface flatness and uniformity. g–i) SEM images of thinner CsSnBr$_3$ film. g) Lower magnification image of the CsSnBr$_3$/NaCl cross section. With the film thickness reduced to around 200 nm, the coverage and flatness are still preserved. The inset shows the camera image of the film investigated and a much lighter color can be seen. h) A tilted cross-section view and i) magnified cross-section view again confirmed the uniform single-crystal deposition. (Scale bar: (d) 30 µm, (e–g) 5 µm, (h) 2 µm, and (i) 500 nm.)

centimeter (substrate size limited) and thickness from nanometers scale to micrometers can be obtained that displays superior carrier dynamics unveiled before. The time-resolved optical characterization has revealed hot photoluminescence (PL) process in the inorganic VPE film which was only observed in hybrid perovskite before. A gigahertz oscillation explained by photo-Dember effect was observed in VPE CsPbBr$_3$ film which is believed as a consequence of the discrepancy in carrier mobilities and long carrier lifetimes.

The VPE growth (see Materials and Methods in the Supporting Information for detailed setup) and characterization results of CsPbBr$_3$/CsSnBr$_3$ thin film are displayed in **Figure 2**. The θ-2θ X-ray diffraction (XRD) scan together with the camera images of the perovskite film are displayed in Figure 2a. The mirror-like reflecting surface of the thin film on a 1 cm × 1 cm NaCl substrate demonstrates the exceptional uniformity and smoothness achieved during growth. The X-ray diffraction result further proves that only (001) and its higher order peaks of the perovskite are present. The Sn-based perovskite exhibits a tiny red shift of peak due to the smaller lattice constant. The rocking curve for the CsSnBr$_3$ (001) is shown as an inset in Figure 2a with the full width at half maximum (FWHM) being 0.11°, another sign of the high film crystallinity. The XRD result for CsPbBr$_3$/NaCl is more complicated in that peak splitting was observed in both (001) and (002), which can be explained by the cubic-orthorhombic phase transition at 130 °C. Since similar splitting is also present in the solution produced bulk single crystal of the same material,[39] the monocrystallinity achieved during high-temperature growth will still hold. The same XRD pattern in logarithmic scale can be found in Figure S1 (Supporting Information), where in addition to the CsSnBr$_3$ result, in CsPbBr$_3$, an almost negligible (011) peak with intensity three orders lower is present. We attribute such peak to the occasional secondary nucleation of (011) ridges on the perovskite surface during the cooling process. To substantiate the single-crystal epitaxy as well as the in-plane epitaxial relation, pole figure characterization of both growth was performed. Figure 2b shows the (110) pole figure of CsSnBr$_3$, with four distinct poles at χ = 45° and each 90° apart in ϕ angle, which fits well with one single-crystal domain of (001)-oriented cubic CsSnBr$_3$. As marked by the coordinate, the in-plane orientation of [010] and [100] can also be determined. With a similar characterization on the substrate NaCl poles (Figure S2, Supporting Information) for the same sample, the relative in-plane relation can be obtained, which turns out to be epitaxial CsSnBr$_3$ [100]||NaCl [100], consistent with our hypothesis in Figure 1a. The lattice mismatch in this case would then be $\varepsilon = \frac{a_{\mathrm{NaCl}} - a_{\mathrm{CsSnBr3}}}{a_{\mathrm{NaCl}}} = -2.85\%$. A similar (111) pole figure for CsPbBr$_3$ on NaCl is shown in Figure 2c. The same four poles with 90° interval were collected, which also point to monocrystallinity across the substrate. However interestingly, the NaCl pole figure (Figure S3, Supporting Information) reveals that unlike the $CsSnBr_3$ case, a 45° in-plane rotation (i.e., $CsPbBr_3$ [110]||NaCl [100]) is found which renders a lattice mismatch of $\varepsilon = \frac{a_{NaCl} - a_{CsPbBr3}}{a_{NaCl}} = -3.72\%$. In both cases, the observation of the film–substrate orientation serves as a sound proof of the epitaxial growth of either $CsSnBr_3$ and $CsPbBr_3$ on the NaCl substrate. To validate such observation, we conducted growth at much higher pressure (≈120 Torr) to evaluate the nucleation of $CsPbBr_3$ on NaCl in the initial stages. Figure S4 (Supporting Information) shows the resultant square $CsPbBr_3$ flake growth, from which based on the square orientations we can see epitaxial growth of three different in-plane configurations: {PVK [100]||NaCl [100], PVK [010]||NaCl [010], {PVK [110]||NaCl [100], PVK [110]||NaCl [010]}, {PVK [100]||NaCl [100], PVK [110]||NaCl [010]}, with the final configuration resulting in the (011) ridge/prism growth. All epitaxial growth can be divided into two kinds of line-on-line relations, that is, [100] on [100] or [110] on [100]. As a tentative explanation, in Figure S5 (Supporting Information) we plotted the atomic arrangements of both $CsPbBr_3$ and NaCl under the two conditions mentioned above. We note that due to the different lattice types, for [100] on [100], an intuitively ideal configuration, only half of the perovskite atoms are bonded on top of a different type of ion (e.g., cation on anion), while the other half sit right on top of the same type, which is thermodynamically unfavorable. The second relation [110] on [100], however, would result in all perovskite atoms in intermediate atomic positions. From our assumption, the total energy benefit for two cases would qualitatively be similar so the observed flake orientation is a statistical result. As the growth rate increases, however, the high mobility of atoms on NaCl substrate would merge different domains into a single one, with the dominant orientation forming the final in-plane relation. In Figure S6 (Supporting Information), we show that at slightly higher nucleation and growth rate, all flakes can be grown in one single orientation, validating our hypothesis and also the epitaxial growth from another aspect. Our understanding of the growth kinetics in VPE would thus enrich the present knowledge based on the development of high-quality halide perovskite material.[40,41] Interestingly, the as-grown square flakes show significant blue shift of PL peak compared to that of thin film and bulk $CsPbBr_3$ (Figure S7, Supporting Information), with additional XRD characterization showing a red shift of (001) peaks for the flake sample (Figure S8, Supporting Information). Both the shift in lattice constant and band gap are solid evidence of Cl diffusion into the flake at initial stage of growth, which provides with additional source for the good wetting between the perovskite and NaCl substrate. However, such trend is not observed for the fast growth of uniform thin film at lower growth pressure, which indicates that no Cl is present in the majority of the thin film. Nonetheless, we do believe that Cl diffusion is still possible at the interface. Such interphase interface diffusion on the other hand could help enable a better wetting chemistry between the substrate and film.

Apart from the epitaxial growth, another important feature for VPE is the ability to control film thickness while preserving surface smoothness. Figure 2d–i further shows the scanning electron microscope (SEM) analysis of the thickness and roughness for both thicker and thinner films. The cross-section view of an ≈8 µm $CsSnBr_3$ thick film on NaCl is displayed in Figure 2d. In addition to the surface smoothness, the perovskite growth is so conformal that the deposition follows exactly the step on the NaCl surface, as marked by the dashed red circle. A magnified view in Figure 2e shows the absence of any grain boundaries and pinholes across the film. A similar condition can be found for the $CsPbBr_3$ case in Figure 2f where for an ≈7 µm thick film, a flat surface and good registration to the substrate can be observed. Figure 2g continues to show a much thinner (≈200 nm) $CsSnBr_3$ film with unchanged uniformity across the 1 cm × 1 cm substrate. Corresponding to the reduced thickness, the camera image shows a much lighter color and certain level of transparency compared with that of Figure 2a. Figure 2h displays a tilted cross-section SEM view of the sample containing both interface and the upper surface, which again confirms the uniformity. A closer look at the interface is presented in Figure 2i where the flat film follows well with the substrate. As a conclusion, with VPE technique, we are able to obtain uniform film with thickness down to a few hundred nanometers, meeting the requirement for many device applications. Using a mixed $SnBr_2/PbBr_2$ precursor, it is also possible to realize the B-site alloying proposed in Figure 1b. The resultant centimeter-scale thin film exhibits gradual color change from orange (pure Pb based) to black (pure Sn based), as shown in Figure S9 (Supporting Information). Despite the uniform color for each composition, the PL spectra in Figure S10 (Supporting Information) show intriguing features that may possibly result from phase separation. Puzzling as the results are to us, they are consistent with previous research on solution-based film.[42]

Optical properties of the as-grown perovskite thin film were further investigated using time-resolved photoluminescence (TRPL) spectroscopy (see Characterizations in the Supporting Information for detailed setup) to verify the hypothesis in Figure 1c. **Figure 3**a shows the TRPL curves under similar excitation for flakes grown on NaCl, mica, and also the thick continuous film (≈10 µm). It can clearly be seen that for flakes with similar lateral dimension and thickness, when grown on NaCl, the lifetime is greatly reduced from 1.9 ns on mica to 470 ps. The reduction could be attributed to the inclusion of Cl element as discussed in Figure 2 and also from the band alignment at the NaCl/perovskite interface since the conduction band minimum of NaCl lies very close to halide perovskite.[43–45] The lifetime for large-scale thick $CsPbBr_3$ film, on the other hand, is prolonged to as much as 30 ns on average for all the samples tested. The results clearly show the improvement of lifetime by eliminating the grain boundary and minimizing interface defects. In **Figure 4**b, we repeated the TRPL analysis at different emission energies and plot the data into a 2D color map, with the color reflecting the relative logarithmic PL intensity. A clear "shoulder" at higher energy from 2.42 to 2.47 eV is found which represents an additional decay above the valley-to-valley transition energy (≈2.4 eV), namely, a hot PL process during the first few hundred picoseconds to a few nanoseconds upon optical pump. For the flake samples on both NaCl and mica, however, no obvious hot PL is collected (Figure S11, Supporting Information). The hot PL in $CsPbBr_3$ film is revealed more straightforwardly as we plot the "transient" PL spectrum after

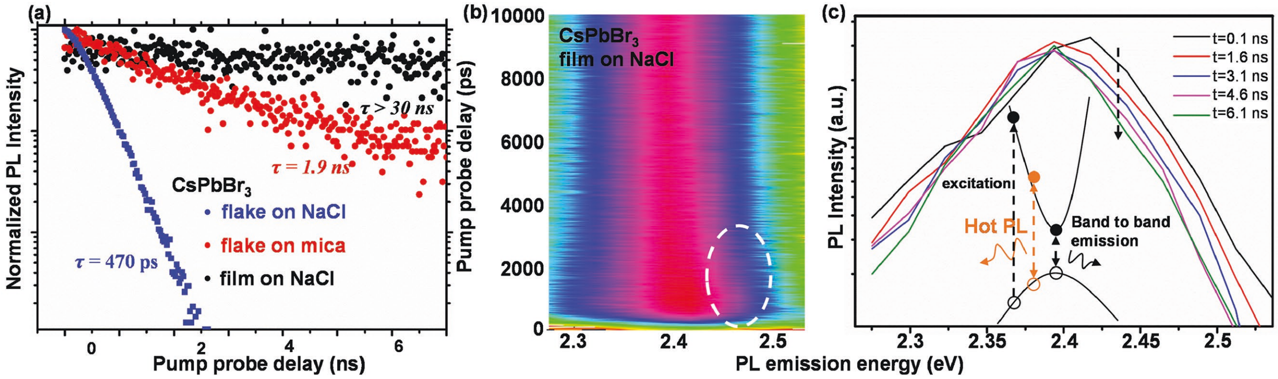

Figure 3. Hot PL in VPE $CsPbBr_3$ film. a) TRPL curves at PL peak energy for $CsPbBr_3$ flakes on NaCl (blue), flakes on mica (red), and film (black) with film sample showing a much prolonged lifetime for more than 30 ns. b) 2D color map for TRPL of $CsPbBr_3$ thick film at different PL emission energies. A shoulder (marked by white dashed circle) at higher energy is obvious which corresponds to the hot PL cooling process. c) Transient PL spectra after optical pumping of the same sample as in (b), with an interval of 1.5 ns for each curve displayed. Hot PL is more easily visible at above-band-gap energies that cool down in a few nanoseconds. The inset schematic shows the process of absorption, hot PL, and normal band-to-band emission upon laser excitation.

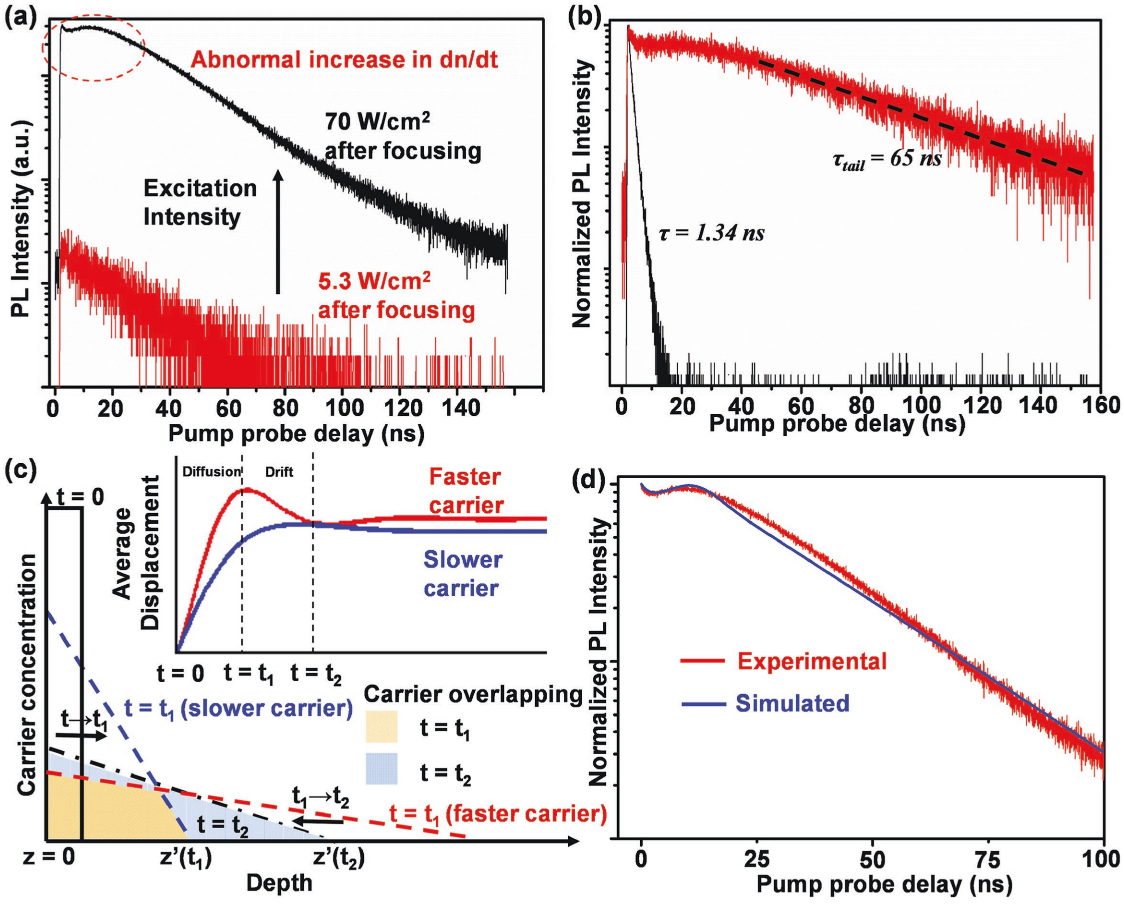

Figure 4. Photo-Dember effect in VPE $CsPbBr_3$ film on NaCl. a) Excitation intensity dependent TRPL for a thick $CsPbBr_3$ film showing abnormal oscillation for larger excitation intensity (black). The TRPL tail, however, gives a similar decay rate for both cases. The laser intensity after focusing by the objective lens is labeled for both cases. b) TRPL curves for a thinner film (black) and thicker film (red) with same lateral coverage and excitation intensity. The thicker film has both an abnormal oscillation and a much slower decay tail equivalent to a lifetime of 65 ns. c) Illustration of the electron–hole concentration profile along the film thickness direction at different times after excitation. The carriers are first separated by their intrinsic different diffusivity and later pulled back by the electric field (dipole) generated due to separation. During the entire process, carrier overlapping changes overtime, as marked by the shaded area. The different trajectories of faster and slower carrier are depicted in the inset with the aid of a damped cosine function. d) Comparison between the simulated TRPL curve (blue) versus experiment data (red).

every 1.5 ns in Figure 3c. The long-lived hot charges lasted for a significant duration prior to being cooled to the band valleys, which is also shown by the schematics as an inset. Hot PL was recently collected in organic–inorganic hybrid halide perovskite single-crystalline flakes but not in pure inorganic ones.[46] In a broader point of view, the hot PL should exist in almost all direct band gap materials given an above band gap excitation. Statistically, the hot electron and holes will recombine and give hot PL at the same time of their thermal relaxation to the band valley. As an example, hot PL has been long discovered in traditional semiconductors like GaAs[47] and GaN.[48] The quality of crystal (i.e., defect and trap states, grain boundaries) would determine the detectability of the hot PL in terms of time scale. In other words, the hot PL in bad-quality crystals is too short lived for the instrument to resolve. Based on these arguments, we believe that the hot PL previously found for hybrid perovskite would still be detected in pure inorganic perovskite given a much enhanced quality, and this is where the high-temperature VPE could be advantageous. Since hot PL is detected in micrometer-sized $MAPbBr_3$ flakes but not in $CsPbBr_3$ flakes, our findings in Figure 3 are consistent with that of Zhu et al. At the same time, we also show that given the lifetime long enough, hot PL cooling is also detectable in inorganic halide perovskites thin film. Our results also indirectly agree with the conclusion from Zhu et al. that the $CH_3NH_3^+$ groups provide additional contribution to the hot PL making them significant even in the micrometer-sized flakes. In other words, the loss of such additional contribution in inorganic perovskite is compensated by the higher crystal quality (overall longer lifetime) in our $CsPbBr_3$ film.

The VPE film and its long lifetime on the other hand also provide ample space for substantial diffusion of charge carriers. To study this, we increased the excitation fluence and found very intriguingly the unexpected TRPL curve shown in Figure 4a. As the fluence increases (≈70 W cm^{-2} after microscope focusing), the curve (black) showed an abnormal oscillation in the first ≈15 ns, while the "tail" of the curve follows well with the low excitation scenario (red, ≈5.3 W cm^{-2} after microscope focusing), entailing a similar lifetime. From the abnormal shape, the curve exhibits an increase of PL accounts at the "bump" and would not be well fitted by simple addition of monoexponential decays. Also due to the fact that the anomalous bump only occurs at higher laser intensity (which in turn gives PL counts with high signal-to-noise ratio), it is very unlikely that the noise of the light source results in the bump. We also note that such phenomenon exists exclusively in thicker (≈10 µm) film with relatively high level of excitation. Shown in Figure 4b is comparison of TRPL curves for thinner (≈1 µm) and thicker (≈10 µm) films and affected by the interfaces and excitation level, thinner one displays a much reduced lifetime regardless of the lateral dimension. Apart from a different shape, the thicker film renders an effective lifetime at the tail for as long as 65 ns, the longest to the best of our knowledge in $CsPbBr_3$ material. The abnormal increase in TRPL means more radiative recombination of e^--h^+ pairs with time, which could be possible for two reasons: (1) as carriers diffuse deeper into the material, a higher PL quantum yield (PLQY) compensates for the concentration decay; (2) electron and holes diffuse with different rates and their overlapping in concentration profile varies with time. The latter hypothesis, also known as the photo-Dember effect, would be necessary for the oscillation to be observed, whereas the first is only expected to create a "bump" in the initial stage. The photo-Dember effect[49] in short depicts that electrons and holes would be separated in the initial stage due to the different diffusivity, thus creating an electric field, which in turn would attract the carriers and cause the reunion.[50,51] The time and spatial scale for the oscillation process to happen depends on the absolute diffusivity as well as the net difference between the two types. Due to the fact that single-crystalline halide perovskite has mobility[17,18] (at an order of 100 $cm^2\ V^{-1}\ s^{-1}$) about orders lower than traditional III–V materials but much longer lifetime, it is therefore reasonable for the oscillation to take place in nanosecond regime over a depth of several micrometers. Moreover, difference in carrier mobility has been already reported in multiple hybrid halide perovskite studies.[23,52] As a clearer illustration, we modeled the electron–hole diffusion-drift process semiquantitatively in Figure 4c. Initially at $t = t_0$ (t: time; t_0: the time of optical pumping), the optical pumping would inject a high electron–hole concentration with electron/hole fully spatially overlapped near the sample surface. At later time, we approximate the concentration profile of both electrons and holes as a triangle as a first-order approximation. The triangle assumption would be valid as it, to a great extent, fits the recent study on carrier diffusion in halide perovskite[37] as well as past simulation work on the photon-Dember effect.[53] At $t = t_1$ (t_1: the time lapsed after optical pumping), the discrepancy in diffusivity of electron and hole resulted in the largest separation of the two types of carriers, with the carrier overlapping marked as the orange shaded area. For $t > t_1$, the drifting process caused by the electric fields dominates, causing the electrons and holes to move toward each other and therefore at $t = t_2$ (t_2: the time lapsed after optical pumping), an overall larger overlapping compared with t_1 takes place. To further quantify such change, we adopted a damped cosine curve to simulate the average displacement (i.e., the center of the triangle) of the faster and slower carriers

$$l_{\text{fast}} = A_1\left(1-\cos\left(\frac{t}{T}\cdot 2\pi\right)\right)\cdot\exp\left(\frac{-t}{\tau_{\text{a}}}\right) \tag{2}$$

$$l_{\text{slow}} = A_2\left(1-\cos\left(\frac{t}{T}\cdot \pi\right)\right)\cdot\exp\left(\frac{-t}{\tau_{\text{a}}}\right) \tag{3}$$

where A_1 and A_2 are proportional constants relating the maximum displacement, which can be determined by the diffusivity (mobility) of the carrier, namely, $l_{\text{fast}}\left(\frac{T}{2}\right)\approx\sqrt{\frac{D_{\text{fast}}T}{2}}$. T is the period for the oscillation to take place and τ_{a} a damping constant. Inset of Figure 4c therefore shows the modeled displacements of two carriers. With the assumptions above and a first-order defects mediated and second-order bimolecular recombination for photoexcited carriers, we can determine the decay of overall carrier number at time t by solving the following differential equation

$$N(t) = N(t-\mathrm{d}t) - \frac{N(t-\mathrm{d}t)}{\tau_{\text{nonrad}}}\mathrm{d}t - b(N'_{t-\mathrm{d}t})^2\,\mathrm{d}t \tag{4}$$

where the overlapped carrier number, $N'_{t-\mathrm{d}t}$, can be obtained by integrating the overlapped region at time $t - \mathrm{d}t$. τ_{nonrad} denotes the nonradiative defects determined lifetime and b the second-order recombination coefficient, containing both radiative and nonradiative terms.[54,55] τ_{nonrad} is a thickness (z) dependent function that increases but finally converges with increasing diffusion depth.[54] With $N(t)$ available and the triangle profile assumption, the resultant carrier profile $n_{\mathrm{fast(slow)}}(z,t)$ for either fast or slow one along thickness direction (z) would then be determined.

The collected PL intensity at time t would therefore be determined from the product of overlapped carriers and the second-order radiative recombination coefficient (the excitation fluence is so high that intrinsic bulk doping is negligible)

$$PL(t) = b_{\mathrm{rad}}\left(N'_{t-\mathrm{d}t}\right)^2 \tag{5}$$

where $b_{\mathrm{rad}}(z)$ is the thickness-dependent second-order radiative recombination coefficient.[54,55] As further away from the surface, the decrease in trap states would entail a reduced second-order nonradiative recombination coefficient[54–56] and reasonably a higher $b_{\mathrm{rad}}(z)$. Per this reasoning, we assume an exponential recombination coefficient function $b_{\mathrm{rad}}(z)$ that converges to a fixed value as the thickness increases, which can be found in Figure S12 (Supporting Information). The specific parameter is obtained by fitting to the measured data. With a combination of the equations above, we plot the simulated TRPL curve with the experimental data in Figure 4d and found the two matches well for both the gigahertz oscillation and a long tail of monoexponential decay. The tiny discrepancy during the oscillation could result from our simplification of the carrier displacement in Equations (2) and (3). The fitted curve is plotted under $T = 18$ ns obtained through our experiment and carrier mobilities approximated based on recent reports on their hybrid counterparts.[17,18] The photo-Dember effect proves that, with a high-quality VPE perovskite film, charge carriers are able to diffuse within nanoseconds over a long distance and still end up with radiative recombination, a significant sign for the future application of perovskite toward high-power electro-optic devices.

In conclusion, by employing VPE and with alkali halide as substrate, we have achieved centimeter-scale single-crystalline thin film for inorganic halide perovskites $\mathrm{ABX_3}$ and their alloys. Substantiated by structural analysis, the as-grown thin film exhibits excellent crystallinity and epitaxial relation with the NaCl substrate. VPE-based inorganic halide perovsite film has shown unprecedented optoelectronic quality, evidenced by the observation of the hot PL process and long period photo-Dember effect. High-temperature processing and epitaxy are believed to be two crucial factors responsible for the superior carrier dynamics of these VPE films. The alkali halide could be universally applied as a unique substrate for the entire halide perovskite family for the VPE growth. The analogy between our VPE of halide perovskite compounds/alloys and the sophisticated III–V field may promise our technique in a vast realm of coherent perovskite heterostructure devices for high-power electro-optic devices.

Supporting Information

Supporting Information is available from the Wiley Online Library or from the author.

Acknowledgements

Y.W., Z.C., and J.S. were supported by NSF Awards under CMMI 1550941 and CMMI 1635520. Y.Y.S and S.B.Z acknowledge support by NSF Award under CBET-1510948. X.S. was supported by the NYSTAR Focus Center at RPI, C130117. The authors sincerely thank Prof. Rafael Jaramillo at Massachusetts Institute of Technology for providing us his insightful understanding on explaining the carrier dynamics of the VPE film. J.S. and Y.W. conceived the study. Y.W. grew the materials, performed the spectroscopy and microscopy characterization, and conducted theoretical analysis. X.S. carried out the X-ray diffraction and pole figure study. All the authors discussed the results and wrote the manuscript.

Conflict of Interest

The authors declare no conflict of interest.

Keywords

epitaxy, halides, perovskites, vapor phase

Received: May 11, 2017

---

[1] N.-G. Park, M. Grätzel, T. Miyasaka, K. Zhu, K. Emery, *Nat. Energy* **2016**, *1*, 1.
[2] M. D. McGehee, *Nat. Mater.* **2014**, *13*, 9.
[3] M. A. Green, A. Ho-Baillie, H. J. Snaith, *Nat. Photonics* **2014**, *8*, 7.
[4] S. Adachi, *Properties of Semiconductor Alloys: Group-IV, III-V and II-VI Semiconductors*, Vol. *28*, Wiley, New York **2009**.
[5] G. E. Eperon, G. M. Paterno, R. J. Sutton, A. Zampetti, A. A. Haghighirad, F. Cacialli, H. J. Snaith, *J. Mater. Chem. A* **2015**, *3*, 39.
[6] N. J. Jeon, J. H. Noh, Y. C. Kim, W. S. Yang, S. Ryu, S. I. Seok, *Nat. Mater.* **2014**, *13*, 9.
[7] M. Liu, M. B. Johnston, H. J. Snaith, *Nature* **2013**, *501*, 7467.
[8] NREL Solar Cell Efficiency Record Chart, http://www.nrel.gov/ncpv/images/efficiency_chart.jpg (accessed: October 2016).
[9] S. W. Eaton, M. Lai, N. A. Gibson, A. B. Wong, L. Dou, J. Ma, L.-W. Wang, S. R. Leone, P. Yang, *Proc. Natl. Acad. Sci. USA* **2016**, *113*, 8.
[10] H. Zhu, Y. Fu, F. Meng, X. Wu, Z. Gong, Q. Ding, M. V. Gustavsson, M. T. Trinh, S. Jin, X. Y. Zhu, *Nat. Mater.* **2015**, *14*, 6.
[11] Z.-K. Tan, R. S. Moghaddam, M. L. Lai, P. Docampo, R. Higler, F. Deschler, M. Price, A. Sadhanala, L. M. Pazos, D. Cregdington, *Nat. Nanotechnol.* **2014**, *9*, 9.
[12] C. C. Stoumpos, C. D. Malliakas, J. A. Peters, Z. Liu, M. Sebastian, J. Im, T. C. Chasapis, A. C. Wibowo, D. Y. Chung, A. J. Freeman, B. W. Wessels, M. G. Kanatzidis, *Cryst. Growth Des.* **2013**, *13*, 7.
[13] H. Wei, Y. Fang, P. Mulligan, W. Chuirazzi, H.-H. Fang, C. Wang, B. R. Ecker, Y. Gao, M. A. Loi, L. Cao, J. Huang, *Nat. Photonics* **2016**, *10*, 333.
[14] S. Nakamura, *Rev. Mod. Phys.* **2015**, *87*, 4.
[15] J.-F. Ge, Z.-L. Liu, C. Liu, C.-L. Gao, D. Qian, Q.-K. Xue, Y. Liu, J.-F. Jia, *Nat. Mater.* **2015**, *14*, 3.
[16] A. Cho, *Thin Solid Films* **1983**, *100*, 4.
[17] Y. Fang, Q. Dong, Y. Shao, Y. Yuan, J. Huang, *Nat. Photonics* **2015**, *9*, 679.
[18] Q. Dong, Y. Fang, Y. Shao, P. Mulligan, J. Qiu, L. Cao, J. Huang, *Science* **2015**, *347*, 6225.

[19] M. I. Saidaminov, A. L. Abdelhady, B. Murali, E. Alarousu, V. M. Burlakov, W. Peng, I. Dursun, L. Wang, Y. He, G. Maculan, *Nat. Commun.* **2015**, *6*, 7586.

[20] M. I. Saidaminov, M. A. Haque, J. Almutlaq, S. Sarmah, X.-H. Miao, R. Begum, A. A. Zhumekenov, I. Dursun, N. Cho, B. Murali, *Adv. Opt. Mater.* **2016**, *5*, 1600704.

[21] Y. Chen, M. He, J. Peng, Y. Sun, Z. Liang, *Adv. Sci.* **2016**, *3*, 4.

[22] Y.-X. Chen, Q.-Q. Ge, Y. Shi, J. Liu, D.-J. Xue, J.-Y. Ma, J. Ding, H.-J. Yan, J.-S. Hu, L.-J. Wan, *J. Am. Chem. Soc.* **2016**, *138*, 16196.

[23] W. Peng, L. Wang, B. Murali, K.-T. Ho, A. Bera, N. Cho, C.-F. Kang, V. M. Burlakov, J. Pan, L. Sinatra, C. Ma, W. Xu, D. Shi, E. Alarousu, A. Goriely, J.-H. He, O. F. Mohammed, T. Wu, O. M. Bakr, *Adv. Mater.* **2016**, *28*, 3383.

[24] Y. Peter, M. Cardona, *Fundamentals of Semiconductors: Physics and Materials Properties*, Springer Science & Business Media, Berlin, Germany, **2010**.

[25] Y. Wang, Y. Shi, G. Xin, J. Lian, J. Shi, *Cryst. Growth Des.* **2015**, *15*, 10.

[26] Y. Wang, X. Sun, R. Shivanna, Y. Yang, Z. Chen, Y. Guo, G.-C. Wang, E. Wertz, F. Deschler, J. Shi, *Nano Lett.* **2016**, *16*, 12.

[27] J. Chen, Y. Fu, L. Samad, L. Dang, Y. Zhao, S. Shen, L. Guo, S. Jin, *Nano Lett.* **2016**, *17*, 460.

[28] K. Müller, C. Chang, *Surf. Sci.* **1968**, *9*, 3.

[29] M. Odelius, M. Bernasconi, M. Parrinello, *Phys. Rev. Lett.* **1997**, *78*, 14.

[30] P. Cottingham, R. L. Brutchey, *Chem. Commun.* **2016**, *52*, 30.

[31] L. Protesescu, S. Yakunin, M. I. Bodnarchuk, F. Krieg, R. Caputo, C. H. Hendon, R. X. Yang, A. Walsh, M. V. Kovalenko, *Nano Lett.* **2015**, *15*, 6.

[32] L.-Y. Huang, W. R. Lambrecht, *Phys. Rev. B* **2013**, *88*, 16.

[33] E. T. Hoke, D. J. Slotcavage, E. R. Dohner, A. R. Bowring, H. I. Karunadasa, M. D. McGehee, *Chem. Sci.* **2015**, *6*, 1.

[34] E. Unger, E. T. Hoke, C. D. Bailie, W. H. Nguyen, T. Humuller, A. R. Bowring, M. G. Christoforo, M. D. McGehee, *Energy Environ. Sci.* **2014**, *7*, 11.

[35] Y. Shao, Z. Xiao, C. Bi, Y. Yuan, J. Huang, *Nat. Commun.* **2014**, *5*, 5784.

[36] A. Sproul, *J. Appl. Phys.* **1994**, *76*, 5.

[37] Y. Yang, Y. Yan, M. Yang, S. Choi, K. Zhu, J. M. Luther, M. C. Beard, *Nat. Commun.* **2015**, *6*, 7961.

[38] H.-H. Fang, S. Adjokatse, H. Wei, J. Yang, G. R. Blake, J. Huang, J. Even, M. A. Loi, *Sci. Adv.* **2016**, *2*, 7.

[39] Y. Rakita, N. Kedem, S. Gupta, A. Sadhanala, V. Chalchenko, M. L. Bolm, M. Kulbak, R. H. Friend, D. Cahen, G. Hodes, *Cryst. Growth Des.* **2016**, *16*, 10.

[40] Y. C. Zheng, S. Yang, X. Chen, Y. Chen, Y. Hou, H. G. Yang, *Chem. Mater.* **2015**, *27*, 14.

[41] S. Yang, Y. C. Zheng, Y. Hou, X. Chen, Y. Chen, Y. Wang, H. Zhao, H. G. Yang, *Chem. Mater.* **2014**, *26*, 23.

[42] F. Hao, C. C. Stoumpos, R. P. Chang, M. G. Kanatzidis, *J. Am. Chem. Soc.* **2014**, *136*, 22.

[43] R. Poole, J. Liesegang, R. Leckey, J. Jenkin, *Phys. Rev. B* **1975**, *11*, 12.

[44] P. Schulz, E. Edri, S. Kirmayer, G. Hodes, D. Cahen, A. Kahn, *Energy Environ. Sci.* **2014**, *7*, 4.

[45] C. Wang, B. R. Ecker, H. Wei, J. Huang, J. Q. Meng, Y. Gao, *Phys. Chem. Chem. Phys.* **2016**, *19*, 5361.

[46] H. Zhu, K. Miyata, Y. Fu, J. Wang, P. P. Joshi, D. Niesner, K. W. Williams, S. Jin, X. Y. Zhu, *Science* **2016**, *353*, 6306.

[47] D. Mirlin, I. J. Karlik, L. Nikitin, I. Reshina, V. Sapega, *Solid State Commun.* **1981**, *37*, 9.

[48] F. Binet, J. Duboz, J. Off, F. Scholz, *Phys. Rev. B* **1999**, *60*, 7.

[49] H. Dember, *Phys. Z.* **1931**, *32*, 554.

[50] P. Gu, M. Tani, S. Kono, K. Sakai, X.-C. Zhang, *J. Appl. Phys.* **2002**, *91*, 9.

[51] K. Liu, J. Xu, T. Yuan, X.-C. Zhang, *Phys. Rev. B* **2006**, *73*, 15.

[52] Z. Chen, Y. Wang, Y. Shi, B. Hsu, Z. Yang, J. Shi, *Adv. Electron. Mater.* **2016**, *2*, 10.

[53] M. B. Johnston, D. Whittaker, A. Corchia, A. Davies, E. H. Linfield, *Phys. Rev. B* **2002**, *65*, 16.

[54] P. T. Landsberg, *Recombination in Semiconductors*, Cambridge University Press, Cambridge, UK, **1992**.

[55] J. M. Richter, M. Abdi-Jalebi, A. Sadhanala, M. Tabachnyk, J. P. H. Rivett, L. M. Pazos-Outon, K. C. Godel, M. Price, F. Deschler, R. H. Friend, *Nat. Commun.* **2016**, 7.

[56] K. Zheng, K. Zidek, M. Abdellah, M. E. Messing, M. J. Al-Marri, T. Pullerits, *J. Phys. Chem. C* **2016**, *120*, 5.